

Micromodel of a Gas Diffusion Electrode Tracks In-Operando Pore-Scale Wetting Phenomena

Anna M. Kalde, Maren Grosseheide, Sebastian Brosch, Sharon V. Pape, Robert G. Keller, John Linkhorst, and Matthias Wessling*

Utilizing carbon dioxide (CO₂) as a resource for carbon monoxide (CO) production using renewable energy requires electrochemical reactors with gas diffusion electrodes that maintain a stable and highly reactive gas/liquid/solid interface. Very little is known about the reasons why gas diffusion electrodes suffer from unstable long-term operation. Often, this is associated with flooding of the gas diffusion electrode (GDE) within a few hours of operation. A better understanding of parameters influencing the phase behavior at the electrolyte/electrode/gas interface is necessary to increase the durability of GDEs. In this work, a microfluidic structure with multi-scale porosity featuring heterogeneous surface wettability to realistically represent the behavior of conventional GDEs is presented. A gas/liquid/solid phase boundary was established within a conductive, highly porous structure comprising a silver catalyst and Nafion binder. Inoperando visualization of wetting phenomena was performed using confocal laser scanning microscopy (CLSM). Non-reversible wetting, wetting of hierarchically porous structures and electrowetting were observed and analyzed. Fluorescence lifetime imaging microscopy (FLIM) enabled the observation of reactions on the model electrode surface. The presented methodology enables the systematic evaluation of spatio-temporally evolving wetting phenomena as well as species characterization for novel catalyst materials under realistic GDE configurations and process parameters.

is the electrification of production processes for fuels and commodity chemicals,^[1,2] utilizing renewably generated energy. Many of these processes rely on multi-phase reactions in gas diffusion electrodes (GDE) bringing a solid, a liquid, and a gaseous phase into contact. In conventional electrochemical cells, poor gas solubility and limited active surface area at the solid surfaces prevent high conversion rates. In contrast, the use of porous gas diffusion electrodes allows for enhanced electrode surface area, enlarged ternary phase boundaries, and elevated mass transport.^[3–5]

Over the past decades, GDEs have been successfully employed in electrochemical processes to overcome diffusion and solubility limitations in multi-phase reactions. GDEs are currently used in diverse processes such as in fuel cells,^[6] chlor-alkali electrolysis,^[7] H₂O₂ production,^[8] and electrochemical CO₂ reduction.^[3–5,9] In this work, we aim to access spatio-temporal details of the wetting and reaction phenomena at the three phase boundary for electrochemical carbon dioxide CO₂ reduction.

GDEs consist of a hydrophobic, porous, and conductive material that provides mechanical stability, is permeable for gases, guarantees electron transport and enables reduction or oxidation reactions. Gas is provided from one side through the GDE. On the other side, it is contacted with a liquid electrolyte providing the protons which are necessary for CO₂ reduction. The liquid-facing side of the GDE is equipped with a catalyst layer for targeted reduction reactions.^[3] Electrical potential for reaction induction is applied between the GDE and a counter electrode confining the liquid phase. Typically, the liquid-filled chamber between the electrodes is divided into two compartments using an ion-conducting membrane. For a more detailed description of different electrochemical cell designs using GDEs, the reader is kindly referred to the literature.^[9,10]


In the field of GDEs for CO₂ reduction, substantial work has been presented in the literature on catalyst design,^[11,12] GDE composition,^[13–15] and process studies on laboratory scale.^[16–18] We recently presented a detailed model that predicts speciation and pH gradients for the reduction of CO₂,^[19] and investigated wetting in porous networks comprised of surfaces with different zeta potentials.^[20] Although the fundamental

1. Introduction/State of the Art

In recent years, significant effort has been undertaken to reduce the impact of greenhouse gas emissions. One promising approach

A. M. Kalde, M. Grosseheide, S. Brosch, S. V. Pape, R. G. Keller, J. Linkhorst, M. Wessling
RWTH Aachen University
Aachener Verfahrenstechnik - Chemical Process Engineering
Forckenbeckstr. 51, 52074 Aachen, Germany
E-mail: manuscripts.cvt@avt.rwth-aachen.de

A. M. Kalde, M. Wessling
DWI - Leibnitz Institute for Interactive Materials
Forckenbeckstr. 50, 52074 Aachen, Germany

 The ORCID identification number(s) for the author(s) of this article can be found under <https://doi.org/10.1002/smll.202204012>.

© 2022 The Authors. Small published by Wiley-VCH GmbH. This is an open access article under the terms of the Creative Commons Attribution-NonCommercial-NoDerivs License, which permits use and distribution in any medium, provided the original work is properly cited, the use is non-commercial and no modifications or adaptations are made.

DOI: 10.1002/smll.202204012

understanding of mechanisms in GDEs has drastically improved over the last years and promising studies have been shown on a larger scale, there still is a lack of systematic understanding on dominating effects in GDEs on a multi-pore scale. One major challenge reported for GDEs on the cm^2 scale and above is their performance stability over time.^[21,22] This loss in performance can be associated with the liquid intrusion in the GDE's pores. In turn, this limits the available electrochemically active surface area for reaction and hinders mass transport by increasing diffusive transport resistances.^[22] Additionally, GDE pores can be blocked by salt precipitation from dissolved ions in the liquid solution.^[16,22] Both the flooding of GDE pores and the salt precipitation are expected to depend on local material and process parameters such as pore diameter and geometry, material wettability, concentration gradients and reactions at the electrode, electric driving forces such as electrowetting or the pressure distribution between gas and electrolyte. Hence, a more detailed understanding of these parameters at the meso-scale on a multi-pore level under realistic operating conditions is required to optimize electrolysis processes involving GDEs.

Up until now, few studies investigated GDE wetting and flooding events. The applied potential,^[18] local pressure distribution in the GDE,^[22,23] and the formation of liquid products^[22] alter the local wetting behavior in GDEs. Flooding phenomena were investigated using various methods. For instance, techniques such as scanning electron microscopy (SEM), energy-dispersive X-ray spectroscopy (EDX), X-ray diffraction (XRD), or focused ion beam (FIB)/SEM tomography were used. Post mortem analysis of GDEs after electrolyte breakthrough offers insight into the influence of salt depositions in the pores of the GDE^[24] or the binder material used in the catalyst layer.^[25] Additionally, the influence of the electrode surface structure, in particular the presence of cracks that can act as flooding reservoirs, was analyzed using EDX and inductively coupled plasma mass spectroscopy (ICP-MS).^[26] This way, the structure and composition of used GDEs and salt deposits can also be analyzed.

However, these methods do not allow an analysis of the GDE in operando. With the aid of simulations, mass transport phenomena during electrolysis can be described based on SEM and FIB/SEM images of GDEs.^[25,27] Yet, true in operando analysis of wetting and flooding phenomena remains challenging. Csoklich et al., measured water saturation in novel woven gas diffusion layers using X-ray computed tomography (CT) in operando.^[28] Additionally, operando synchrotron imaging was performed by Paulisch et al., to investigate the electrolyte distribution during chronoamperometry with a time resolution of 1 s.^[29] With these methods, only the liquid phase can be visualized, whereas for CO_2 electroreduction, the triple-phase boundary between the gas, liquid, and solid phase is crucial.^[30] Shi et al., present a method to visualize the phase boundary between CO_2 and electrolyte using fluorescence spectroscopy and a transparent electrolysis cell. They prepared a GDE labeled with a pH-responsive dye, allowing them to track the shift of the phase boundary with changes in the hydrophilicity of the GDE.^[31] With this method, breakthroughs can be observed at the back of the GDE, and post mortem analysis of the GDE enables the visualization of the phase boundary.

The in operando methods described above require extensive instrumentation (synchrotron or X-ray CT) or post-mortem

analysis of electrodes. In addition, reactions and the dynamic development of phase boundaries due to effects such as electrowetting or hierarchically porous structures within a gas diffusion electrode remain challenging to visualize and investigate. The inherent hierarchical porosity of GDEs in combination with the short timescale of single wetting events displays a key challenge for accurate modeling of GDE wetting both in experimental and simulative approaches. Yet, a better understanding of these influences on GDE wetting could lead to an increase in the long-term stability of gas diffusion electrodes during electrolysis, raising the need of in operando analysis in GDE-mimicking systems.

In this study, we develop a precisely tailored micromodel to mimic a GDE structure for electrochemical CO_2 reduction. Using two-photon lithography and soft replica molding, we obtain a hydrophobic and mechanically stable scaffold that is then equipped with a catalytically active layer. This material comprises silver and Nafion and is identical to the material system presented in prior successful studies on GDEs at lab scale.^[9] This way, we achieve a representative system for larger-scale GDEs in terms of material properties and pore sizes, which is controllable under process conditions at a scale of tens of pores. In addition, the micromodel is optically accessible, allowing for in operando analysis via confocal laser scanning microscopy (CLSM) and fluorescence lifetime imaging microscopy (FLIM) of the appropriately labeled liquid phase. Fluorescence lifetime is altered by changes in local characteristics, such as variations in ion concentration,^[32] pH,^[33] temperature,^[34] or electrochemical reactions, as presented in this study. Using FLIM, these changes in characteristic fluorescence lifetime can be resolved spatially and temporally in operando. As a result, we obtain high-resolution information at a pore-scale on the liquid distribution and active reaction areas inside the GDE during operation.

The micromodel developed in this work is a powerful platform for investigating governing mechanisms for wetting and reactions at GDE surfaces. It will instruct the development of larger-scale GDEs for optimizing process conditions and electrode design. Further, we present fluorescent lifetime imaging as a valuable qualitative measurement method to localize active reaction areas in operando and track reaction product movement toward the liquid bulk phase. This work aims to serve as a basis for future studies using the proposed methods for systematically investigating critical parameters in processes using GDEs.

2. Results

2.1. Microfluidic Mimicking Structure

A GDE micromodel was designed to mimic the porous structure of a gas diffusion electrode. It consists of two channels separated by a hexagonally packed homogeneous pillar array. These two channels represent the gas and electrolyte flow field in an electrochemical cell, respectively. The pillar array mimics the pore structure of the GDE. For industrially deployed GDEs, pore sizes vary between 0.001 μm in the catalyst layer (CL) and the microporous layer (MPL), to 500 μm in the macroporous

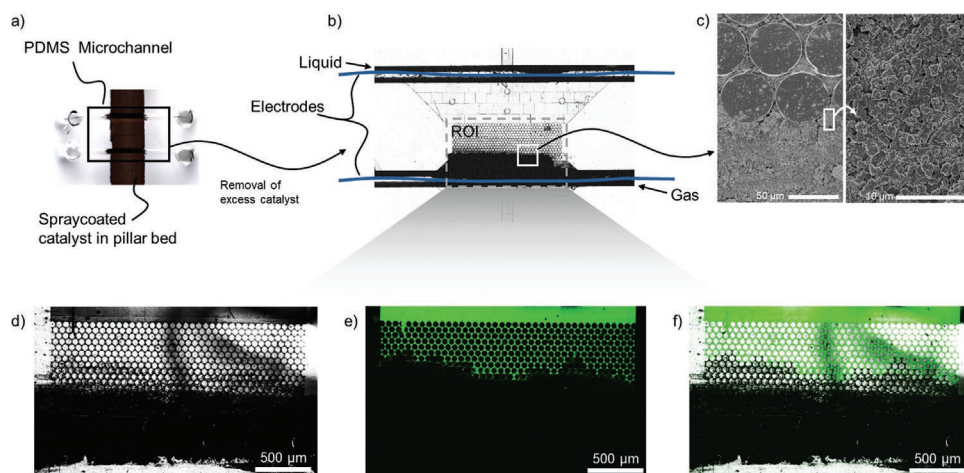


Figure 1. Microchannel designed for wetting experiments. a) Electrode channels coated with catalyst. b) Assembled microchip with electrodes indicated in blue. The region of interest (ROI), which will be shown in all future CLSM and FLIM images, is marked. c) FE-SEM images of the pillar structure and porous catalyst structure. Micrographs of the ROI showing a partially wetted pillar bed regarding d) transmission, e) CLSM fluorescence intensity, and f) the overlay of these two.

substrate (MPS).^[5,35] Not all GDEs are made of three layers; a combined MPL and CL is also possible.^[36] In the microfluidic chip developed in this work, the basic structure's pore size is determined by the inter-pillar spacing, which is set at 2 μm with a pillar diameter of 50 μm . Thus, the governing pore size of this basic microfluidic chip ranges between the common pore sizes of CL and MPS.^[5,35] Pore sizes are further reduced with the application of a catalyst ink, resulting in material and porosity characteristics in the range of large-scale GDE's CLs. The pillar array has an overall dimension of 2000 μm by 680 μm and a height of 5 μm . In **Figure 1a,b**, a microscopy image of the chip is shown, with the gas and liquid channels indicated. Further information about the channel structure and a detailed schematic can be found in Figure S7, Supporting Information.

The microchannel and the pillars are fabricated from polydimethylsiloxane (PDMS), which has a hydrophobic surface, thereby modeling the hydrophobic properties of carbon fiber-based gas diffusion layers. Furthermore, the pores between the PDMS pillars are filled with a silver catalyst previously developed in the group.^[9] Thus, the pillar array accurately represents not only the porous surface structure but also the conductive and catalytic properties of conventional GDEs. To contact the pillar array and as a counter electrode, wire electrodes are integrated into the gas and liquid channels of the chip. The wire in the liquid channel acts as the anode, while the wire in the gas channel directly contacts the catalyst and the pillar array, serving as the cathode.

As depicted in **Figure 1a**, the catalyst layer was applied via spray-coating and the excess was removed prior to further assembly, as described in detail in Section 4. Electron microscopy showed the successful deposition of a thin catalyst layer in the space between the PDMS pillars (compare **Figure 1c**). In addition, the different pore scales of the catalyst particles and the inter-pillar spacing can be observed in these images.

Confocal laser scanning microscopy (CLSM) and fluorescence lifetime imaging microscopy (FLIM) were used to investigate wetting phenomena. Conventional light microscopy is insufficient to visualize thin layers of liquid, especially within

the catalyst-filled pores. The region of interest (ROI) indicated in **Figure 1b** is depicted in all future images. Simultaneously, a transmission image and a CLSM fluorescence intensity image are recorded. From the overlay of both images, the location of the labeled electrolyte and, thus, the wetting front can be determined (compare **Figure 1d–f**). In addition to CLSM, FLIM can be used to visualize changes in the chemical and physical environment in the electrolyte, such as changes in salt concentration, pH, temperature, or even the occurrence of reactions.

Hence, the chip developed in this work allows the accurate deposition of a catalyst material, creating a hierarchically porous structure. The surface properties of the catalyst-filled field of pillars are expected to be the same as a conventional GDE, since an identical catalyst ink was applied to our micro-model as previously published in Vennekoetter (2019).^[9]

2.2. Electrowetting Phenomena

Electrowetting refers to changes in the contact angle of a liquid on a conductive surface upon application of an electrical potential to that surface.^[37] Thus, it is an effect that can also be expected to occur during electrolysis in a GDE. With the developed micromodel, electrowetting phenomena in a GDE can be visualized. **Figure 2a** shows the dominating effect of electrowetting obtained via CLSM analysis. Here, the pore filling rate is plotted over the time of the experiment. The pore filling rate is defined as the number of pores (i.e., spaces surrounded by three pillars) filled in a defined amount of time, compare Section S5, Supporting Information. Exemplary snapshots of in operando visualization are given in **Figure 2b**. While the GDE operates stably (panel A, **Figure 2b**) with a cross-flow configuration of CO_2 and electrolyte without voltage applied, a significant increase in wetting events can be detected once a potential of -1 V is applied (panel B, **Figure 2b**). The potential-induced increase in wetting events eventually results in a liquid breakthrough (panel C, **Figure 2b**) and progresses in further lateral GDE wetting. The accelerated wetting is reversed after the

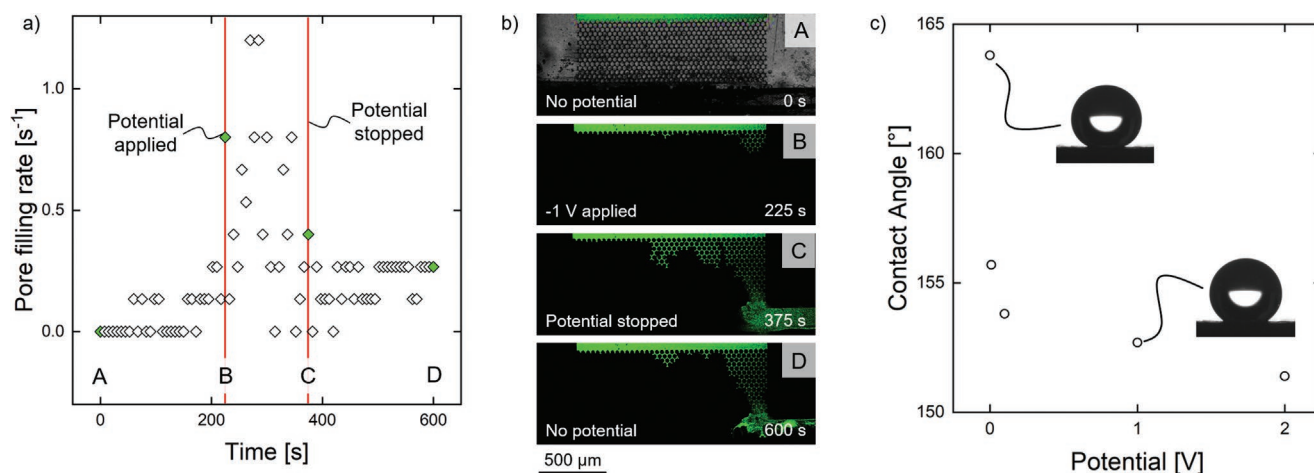


Figure 2. Electrowetting of the pillar bed at an electrical potential of 1 V. a) Pore filling rate over time with and without applied potential. Significant entries are shown in (b) as CLSM images and are referenced with letters (A–D). All experiments shown here are purely driven by electrical potential, no pressure differential was applied between electrolyte and gas channel. c) Contact angle of electrolyte droplets at different applied voltages on a flat GDE sample. A clear decrease in the contact angle with rising voltage can be observed. Electrowetting can be observed via contact angle measurements at potentials as low as 0.01 V.

potential is stopped (panel D, Figure 2b). The corresponding current measured during the experiment is given in Section S1, Supporting Information.

The observed increase in wetting events for the period of the applied voltage is caused by a decrease in contact angle between the electrolyte and the GDE solid matrix. This correlation is confirmed by the static contact angle measurements of electrolyte on a flat GDE surface, spray-coated using the same catalyst ink as the micromodel. The absolute values of these externally measured contact angles should, however, only serve as a rough estimation, as effects such as transitions between Cassie–Baxter- and Wenzel-type wetting states on the microscale might have an additional influence within the pore network of the GDE. It has been shown that these effects can stabilize a seemingly hydrophobic wetting state on an intrinsically hydrophilic material,^[38,39] which is also applicable on the rough surface of silver nanoparticles bound with more hydrophilic Nafion ionomer. Static contact angle results are displayed in Figure 2c. These measurements are in good agreement with other literature observations.^[40] Interestingly, even at low applied potentials, a significant change in the contact angle is observed. Considering the Young–Lippmann equation (compare Figure S6, Supporting Information), small changes to the applied voltage should only have small influences on the contact angle. Yet, as stated above, changes in the wetting state between Cassie–Baxter- and Wenzel-type wetting behavior might additionally influence the contact area between the droplet and the GDE, leading to higher perceived changes in the external contact angle. The decrease in static contact angle by more than 10° reduces the Laplace pressure to be overcome for pore filling, thus, reducing wetting resistances. At the same time, the applied hydrodynamic forces remain constant. This fosters the steady wetting of neighboring pores, which ultimately results in a liquid breakthrough.

Our results confirm that electrowetting is a highly relevant effect in GDE operation. Hence, electrowetting might contribute to the destabilization effect at potential onset observed

in larger-scale experiments.^[16] Generally, wetting/dewetting events typically show a hysteresis behavior and often are not fully reversible. Therefore, our results suggest revising initial operation procedures, which often include a stable flow field before potential onset and subsequent adaption of operation conditions. Since the study presented here, aims to serve as a feasibility study for the designed GDE micromodel and the used analysis methods, a systematic parameter study is subject to future studies. However, the micromodel already shows a high potential to investigate the effect of for example, defect structures on electrowetting events in operando. To the best of the authors knowledge, this is the first quantification of electrowetting in operando in a GDE used for CO₂ reduction. With the micromodel, the advancement of the wetting front in a cross-sectional view of the GDE can easily be shown. For silver-based GDEs catalyzing the oxygen reduction reaction, Bienen et al.,^[41] showed the effects of electrowetting in silver-based GDEs with different porosities and binder loadings. However, they could only rely on electrochemical measurements and optical determination of breakthrough points, whereas the presented micromodel gives further insight into the behavior of the wetting front in a cross-sectional view throughout the entire catalyst layer.

2.3. Wetting in Hierarchically Porous GDE

A pore system with hierarchical pore size distribution was incorporated in the GDE micromodel presented in this work. This way, the effect of GDEs' inherent pore gradient of different layers with varying hydrophobicity was monitored. While the liquid-facing side of the pillar array was spray-coated with the catalyst ink, the gas-facing half of the array was kept as its macroporous PDMS scaffold. Spray-coated and non-spray-coated areas are indicated in Figure 3. Thereby, we can monitor the wetting dynamics at the transition of CL (catalyst layer) to MPL (microporous layer, sprayed-coated area)

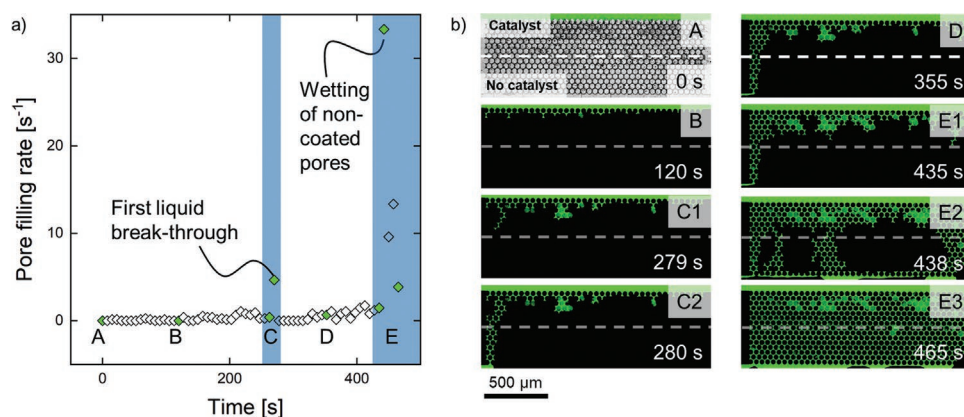


Figure 3. a) Pore filling rate of partially coated pillar bed over time. Two distinct points of liquid breakthrough can be observed. b) Corresponding CLSM images for the marked entries in the graph. As indicated by the dashed line, catalyst particles are deposited in the upper half of the pillar bed. The lower half consists of untreated PDMS. All experiments were performed without an applied potential and are purely pressure driven.

and MPS (macroporous substrate, non-coated area) inside the operating GDE.

To gain insight into the relative wetting dynamics of CL and MPL, a solely pressure-driven experiment was performed without any potential applied to the modified GDE micromodel. Thus, an operating pressure resulting in a slow, steady wetting of the CL was applied. Figure 3 gives the pore filling rate over time with CLSM snapshots at characteristic events.

After a constant slow wetting progression for more than 200 s, the pore-filling rate increases as the liquid front near the liquid inlet approaches the CL to MPL transition zone. Once the CL's rear side is reached, a sudden wetting of the MPL behind is observed, which results in a liquid breakthrough near the gas outlet. Subsequently, wetting in the CL progresses in other areas at a slowly increasing rate. Similar to the first liquid breakthrough, wetting progresses through the CL near the liquid outlet and abruptly wets the MPL once the transition zone is reached. This time, however, the breakthrough near the gas inlet leads to the formation of a liquid layer between the gas channel and the GDE structure as the liquid is pushed along with the gas stream. In turn, this induces a bottom-up wetting of the MPL with the liquid leaking in the gas stream. Eventually, this results in a complete wetting of the GDE structure.

Hence, our results reveal two main observations relevant for larger-scale applications. First, the wetting dynamics between CL and MPL differ by at least one order of magnitude, indicating that the hydrodynamic resistance in the CL is the primary influence on GDE flooding. The hydrophobic surface properties of the MPL and MPS seem to have a comparably small impact, mainly due to the drastically increased pore size of the MPS, leading to reduced hydrodynamic resistance. Second, the location of liquid breakthroughs appears to strongly influence the ensuing GDE wetting phenomena. On the one hand, a breakthrough can eventually foster complete GDE wetting between individual breakthroughs. On the other hand, leaking liquid can be distributed over the gas-downstream GDE area, limiting the area of the GDE accessible for CO_2 and therefore, limiting the GDE performance.

Together with the investigations regarding electrowetting, further insight could be generated into wetting phenomena during electrochemical CO_2 reduction. It should be noted, how-

ever, that these results provide a mainly qualitative analysis of wetting dynamics in GDEs. While trends shown in Figures 2 and 3 were reproducible, challenges for full quantitative reproducibility remain, as chips are only suitable for single use due to residual electrolyte after initial wetting and dewetting.

2.4. Visualizing of Reactions Inside a GDE

Additionally to the visualization of wetting phenomena within the pores of a GDE, the micromodel presented in this work also enables us to visualize localized reactions on the interface between electrode and electrolyte. **Figure 4** shows the direct visualization of active reaction areas obtained via fluorescence lifetime imaging microscopy (FLIM). Local fluorescent lifetimes are indicated via a rainbow scale, brightness is fluorescence intensity-weighted. Initially, the GDE-mimicking structure is flooded with electrolyte solution and shows a spatiotemporally uniform fluorescence lifetime for the entire liquid phase. When a voltage of $U = -10\text{ V}$ is applied, the system immediately forms fluorescence lifetime gradients near the gas-liquid interface. This rapid shift in fluorescence lifetime correlates well with the observed current onset in the system, as given in Section S1, Supporting Information. Hence, the change in fluorescence lifetime must be caused by an electrochemical reaction, either directly or indirectly. Indirect influences on the fluorescent lifetime might be changes in the local pH value, or the formation of ionic species on the electrodes as is often observed with CO_2 electroreduction.^[19,42,43] This reaction visualization via FLIM allows the accurate identification of active areas of the GDE structure.

Under constant applied potential, the gas-liquid interface in the GDE is highly dynamic. We hypothesize that electrowetting phenomena discussed in Section 2.2, as well as gas evolution during a reaction, foster unstable fluid motion. This observation is in good agreement with the literature, reporting stable process conditions prior to voltage onset that destabilize during GDE operation.^[16,22]

In addition to the shift in the characteristic fluorescent lifetime, a divergence of those differently colored areas was observed during the application of the potential (compare

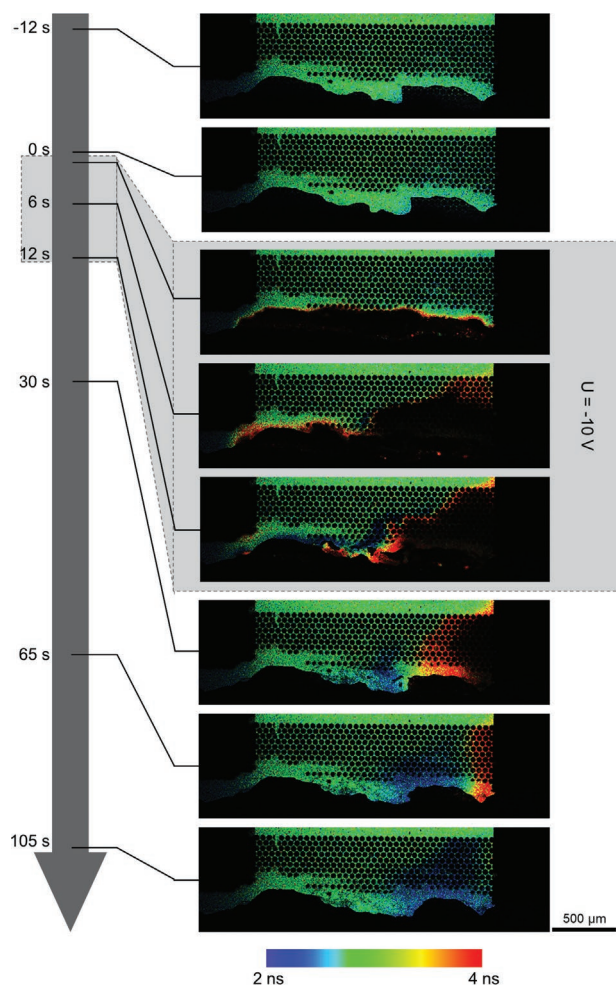


Figure 4. Intensity-weighted fluorescence lifetime images showing a chemical reaction while an electrical potential is applied to a partially wetted pillar bed.

Figure 4, 30 s onward). Thereby, a movement of liquid electrolyte is indicated inside the pillar field from left to right and upward. This movement could be initiated by the convection of the electrolyte being pumped over the pillar field.

While the fluorescence lifetime gradient was nearly constant over the gas–liquid interface length directly after potential onset, three phenomena can be distinguished with the continuing potential application. First, the gas–liquid interface remains mostly stable on the left side of the channel, while the fluorescence lifetime gradient decreases over time. Second, in contrast, the middle part of the channel shows liquid progressing toward the gas bulk phase, where fluorescent lifetime gradients intensify. Third, steeper fluorescence lifetime gradients were also observed in the right side of the channel, where the liquid is receding, and gas is filling most of the pillar array section. This might indicate that moving gas–liquid interfaces during GDE operation could have a beneficial contribution to GDE performance regarding better conditions for the reaction itself, as higher levels of reaction activity were observed for either advancing or receding liquid locations. However, these unstable fluid motions are also expected to promote gas and

liquid breakthroughs, limiting the GDE performance regarding its long-term usability.

Once the potential is switched off, the liquid front stabilizes. In some areas, the altered fluorescence lifetime remains constant, confirming that any change in fluorescence lifetime is caused by either the electrochemical reaction or a parameter directly linked to it. The remaining liquid showing modified fluorescence lifetimes is slowly washed out of the channel in the liquid flow direction.

3. Conclusion

Gas diffusion electrodes are well-established components in various electrochemical processes, such as carbon dioxide reduction. Consisting of a porous conductive structure with reactive centers, gas diffusion electrodes allow for a large contact area for catalyzed gas–liquid reactions with low diffusion transport resistances. Utilizing GDEs in electrolyzers operated with renewable energy offers a powerful approach for the carbon-neutral production of platform chemicals. However, limitations due to electrode flooding, non-uniform flow distribution, and salt precipitation make this prospect challenging. Although research has vastly progressed on understanding gas diffusion mechanisms, questions still remain on in situ kinetics and the effect of pore-scale effects.

For the first time, the study at hand presents a functional microfluidic gas diffusion electrode featuring the same catalyst layer as lab-scale GDEs that can be accessed visually for in operando analysis. Using a PDMS pillar array in combination with an established catalyst ink enables the investigation of liquid distribution and reaction localization within the pores of a GDE.

With this platform, we successfully quantified the influence of electrowetting on phase boundaries within the GDE. We show that the onset of potential in industrial gas-fed electrolyzers might disrupt the previously stable phase boundary. This suggests that stable process conditions need to be found, taking electrowetting into account. In addition, the intrusion behavior of electrolyte solution into hierarchically porous networks with varying wettability was systematically investigated, showing that surface properties of the pores play a subordinate role compared to the pore size. Hence, the successful fabrication of a hierarchically porous structure demonstrates its suitability for future investigations on wetting dynamics in all gas diffusion electrode layers.

In addition, in operando localization of electrochemical reactions in the gas diffusion electrode was performed using fluorescence lifetime imaging microscopy. To the best of the authors' knowledge, this technology is first used in electrochemical reaction mapping in an artificial environment. Future studies will allow parameter studies for both operation parameters and material entities that can be transferred to large-scale devices.

4. Experimental Section

Microfluidic Channel Fabrication: Microfluidic master structures were designed in Autodesk Inventor 2020 and printed with a

Nanoscribe Photonic Professional GT (Nanoscribe GmbH, Eggenstein-Leopoldshafen, Germany) onto standard microscopy slides with IP-S photoresist (Nanoscribe GmbH). SYLGARD 184 silicone elastomer (Dow Chemical, Midland (MI), USA) at a crosslinker:elastomer ratio of 1:10 by weight was cast over the master structures, degassed and cured at 55 °C. The cured channels were removed from the master structure, holes for tubing inlets were punched with biopsy punches and platinum wires (99.9%, diameter 0.05 µm, Goodfellow (Hamburg, Germany)) were inserted into the respective channels. A detailed description of microfluidic chip fabrication is given in Section S2, Supporting Information. The catalyst ink was applied via manual spray-coating using an airbrush pistol (Harder & Steenbeck EVOLUTION Silverline with 0.2 mm nozzle at roughly 3 cm distance to the substrate). The catalyst ink consists of 100 mg silver nanoparticles (50–60 nm, IoLiTec Nanomaterials, Heilbronn, Germany) and 200 µL Nafion (5 wt% fuming FLN-905, Fumatech, Bietigheim-Bissingen, Germany) dispersed in 2 mL each of isopropanol (99.9%, VWR, Radnor (PA), USA) and ultrapure water (from Astacus² water purification device) which were mixed using an ultrasonic bath (Dema Ultrasonic cleaner GT 7810A operated at 42 kHz). A more detailed description is given in Section S3, Supporting Information. After spray-coating, the chips were sintered at 110 °C under vacuum for 1 h. The prepared PDMS channel was then bonded to a microscopy slide (thickness (145 ± 5) µm, Carl Roth, Karlsruhe, Germany) via oxygen plasma activation. Last, the channel is equipped with tubing for fluid control.

For experiments displayed in Section 2.3, half the channel was covered during spray-coating to obtain a two-level porosity over the channel width.

Contact Angle Measurements: Water contact angles were measured on a Krüss DSA100. As the sample, a conventional GDE was prepared by spraycoating the same catalyst ink that was used for microchannel fabrication onto a Freudenberg HC-23 6C gas diffusion layer (Quintec, Göppingen, Germany) and sintering for 1 h at 110 °C under vacuum. Small pieces were cut from the GDE for contact angle analysis. The samples were connected to a Gamry Reference 3000 potentiostat (Gamry, Warminster (PA), USA). Both working and counter electrode were contacted to the GDE, thus, the sample was polarized against the droplet of electrolyte. A droplet of electrolyte solution (1 mol L⁻¹ potassium bicarbonate (≥99.7%, Merck KGaA, Darmstadt, Germany)) was placed on the GDE catalyst side. Contact angles were measured at different applied potentials and evaluated using the Young–Laplace method. A baseline was defined and the droplet shape was numerically approximated using the Young–Laplace equation.

Wetting Experiments and Reaction Visualization: For CLSM and FLIM imaging, a Leica TCS SP8 FALCON system was used. The system's software LAS X SP8 and LAS X FLIM were used for image acquisition and processing. Images were acquired in x–y scan mode with a pulsed laser at 80 MHz pulse frequency using the 488 nm laser line of a white light laser. All CLSM and FLIM images were acquired with an HC PL Fluotar 4x/0.13 lens. For all wetting experiments with the microfluidic chip, a 1 mol L⁻¹ aqueous solution of potassium bicarbonate was used as the electrolyte. For imaging, 0.05 mol L⁻¹ fluorescein sodium salt were added. The electrolyte was pumped through the chip using a Harvard Apparatus PHD Ultra syringe pump. The gas-phase was CO₂ (Air Products GmbH, Hattingen, Germany). Gas flow was controlled using an Alicat Scientific MC series Mass Flow Controller. The exact mass and volume flow rates can be found in Sections S4 and S5, Supporting Information. The given flow rates were not optimized and were chosen carefully to ensure a stable wetting front for each experiment. Liquid flow rates were chosen to represent the conditions found in regular lab-scale flow-cells and gas flow rates were adapted accordingly to ensure stable operation. To apply a potential, a Gamry Reference 3000 potentiostat was used. A schematic and a photographic depiction of the setup are given with annotations in Section S4, Supporting Information. Further information on the visualization methodology and image evaluation can be found in Section S5, Supporting Information.

Electrowetting: For the electrowetting experiments, a gas and liquid flow of 2 mL min⁻¹ and 12 µL min⁻¹, respectively, was set. After

equilibrium was reached, a potential of –1 V was consequently applied. CLSM was used for visualization.

Wetting in Hierarchically Porous GDE: For experiments performed with hierarchically porous GDEs, a gas flow of 2 mL min⁻¹ and electrolyte flow of 30 µL min⁻¹ was set. No potential was applied in these experiments. CLSM was used for visualization.

Reaction Visualization: For reaction visualization, a gas flow of 2 mL min⁻¹ and liquid flow of 10 µL min⁻¹ was set. After equilibrium was reached, a potential of –10 V was applied, and the structure was examined for changes within the liquid phase with FLIM.

Supporting Information

Supporting Information is available from the Wiley Online Library or from the author.

Acknowledgements

A.M.K. and M.G. contributed equally to this work. M.W. acknowledges DFG funding through the Gottfried Wilhelm Leibniz Award 2019 (WE 4678/12-1). M.W. acknowledges the support through an Alexander-von-Humboldt Professorship and the European Research Council (ERC) under the European Union's Horizon 2020 research and innovation program (grant agreement no. 694946). This work was performed in part at the Center for Chemical Polymer Technology CPT, which is supported by the EU and the federal state of North Rhine-Westphalia (grant no. EFRE 30 00 883 02). The authors thank Karin Faensen and Timo Linzenmeier for their support in SEM imaging and contact angle measurement.

Open access funding enabled and organized by Projekt DEAL.

Conflict of Interest

The authors declare no conflict of interest.

Data Availability Statement

The data that support the findings of this study are available from the corresponding author upon reasonable request.

Keywords

gas diffusion electrodes, microfluidics, reaction mapping, wetting

Received: June 29, 2022
Revised: September 28, 2022
Published online: October 17, 2022

- [1] O. S. Bushuyev, P. De Luna, C. T. Dinh, L. Tao, G. Saur, J. van de Lagemaat, S. O. Kelley, E. H. Sargent, *Joule* **2018**, 2, 825.
- [2] P. De Luna, C. Hahn, D. Higgins, S. A. Jaffer, T. F. Jaramillo, E. H. Sargent, *Science* **2019**, 364, 6438.
- [3] D. Higgins, C. Hahn, C. Xiang, T. F. Jaramillo, A. Z. Weber, *ACS Energy Lett.* **2018**, 4, 317.
- [4] T. N. Nguyen, C. T. Dinh, *Chem. Soc. Rev.* **2020**, 49, 7488.
- [5] S. Hernandez-Aldave, E. Andreoli, *Catalysts* **2020**, 10, 713.
- [6] A. Ozden, S. Shahgaldi, X. Li, F. Hamdullahpur, *Prog. Energy Combust. Sci.* **2019**, 74, 50.

- [7] J. Kintrup, M. Millaruelo, V. Trieu, A. Bulan, E. S. Mojica, *Electrochem. Soc. Interface* **2017**, 26, 73.
- [8] J. Wang, C. Li, M. Rauf, H. Luo, X. Sun, Y. Jiang, *Sci. Total Environ.* **2021**, 759, 143459.
- [9] J.-B. Vennekoetter, R. Sengpiel, M. Wessling, *Chem. Eng. J.* **2019**, 364, 89.
- [10] S. Liang, N. Altaf, L. Huang, Y. Gao, Q. Wang, *J. CO₂ Util.* **2020**, 35, 90.
- [11] M. G. Kibria, C.-T. Dinh, A. Seifitokaldani, P. De Luna, T. Burdyny, R. Quintero-Bermudez, M. B. Ross, O. S. Bushuyev, F. P. García de Arquer, P. Yang, D. Sinton, E. H. Sargent, *Adv. Mater.* **2018**, 30, 1804867.
- [12] H. Mistry, Y. W. Choi, A. Bagger, F. Scholten, C. S. Bonifacio, I. Sinev, N. J. Divins, I. Zegkinoglou, H. S. Jeon, K. Kisslinger, E. A. Stach, J. C. Yang, J. Rossmeisl, B. Roldan Cuenya, *Angew. Chem. Int. Ed.* **2017**, 56, 11394.
- [13] E. Antolini, L. Giorgi, A. Pozio, E. Passalacqua, *J. Power Sources* **1999**, 77, 136.
- [14] J. H. Lee, S. Kattel, Z. Xie, B. M. Tackett, J. Wang, C.-J. Liu, J. G. Chen, *Adv. Funct. Mater.* **2018**, 28, 1804762.
- [15] E. W. Lees, B. A. Mowbray, D. A. Salvatore, G. L. Simpson, D. J. Dvorak, S. Ren, J. Chau, K. L. Milton, C. P. Berlinguette, *J. Mater. Chem. A* **2020**, 8, 19493.
- [16] P. Jeanty, C. Scherer, E. Magori, K. Wiesner-Fleischer, O. Hinrichsen, M. Fleischer, *J. CO₂ Util.* **2018**, 24, 454.
- [17] C. Chen, J. F. Khosrowabadi Kotyk, S. W. Sheehan, *Chem* **2018**, 4, 2571.
- [18] K. Yang, R. Kas, W. A. Smith, T. Burdyny, *ACS Energy Lett.* **2021**, 6, 33.
- [19] M. Heßelmann, B. Bräsel, R. Keller, M. Wessling, *Electrochem. Sci. Adv.* **2022**, e2100160, <https://doi.org/10.1002/elsa.202100160>.
- [20] A. Kalde, S. Lippold, J. Loelsberg, A.-K. Mertens, J. Linkhorst, P. A. Tsai, M. Wessling, *Adv. Mater. Interfaces* **2022**, 9, 2101895.
- [21] J.-B. Vennekötter, T. Scheuermann, R. Sengpiel, M. Wessling, *J. CO₂ Util.* **2019**, 32, 202.
- [22] M. E. Leonard, L. E. Clarke, A. Forner-Cuenca, S. M. Brown, F. R. Brushett, *ChemSusChem* **2020**, 13, 400.
- [23] B. De Mot, J. Hereijgers, M. Duarte, T. Breugelmans, *Chem. Eng. J.* **2019**, 378, 122224.
- [24] E. R. Cofell, U. O. Nwabara, S. S. Bhargava, D. E. Henckel, P. J. A. Kenis, *ACS Appl. Mater. Interfaces* **2021**, 13, 15132.
- [25] P. Kunz, M. Paulisch, M. Osenberg, B. Bischof, I. Manke, U. Nieken, *Transp. Porous Media* **2020**, 132, 381.
- [26] Y. Kong, H. Hu, M. Liu, Y. Hou, V. Kolivoška, S. Vesztergom, P. Broekmann, *J. Catal.* **2022**, 408, 1.
- [27] T. Moore, X. Xia, S. E. Baker, E. B. Duoss, V. A. Beck, *ACS Energy Lett.* **2021**, 6, 3600.
- [28] C. Csoklich, R. Steim, F. Marone, T. J. Schmidt, F. N. Büchi, *ACS Appl. Mater. Interfaces* **2021**, 13, 9908.
- [29] M. C. Paulisch, M. Gebhard, D. Franzen, A. Hilger, M. Osenberg, S. Marathe, C. Rau, B. Ellendorff, T. Turek, C. Roth, I. Manke, *ACS Appl. Energy Mater.* **2021**, 4, 7497.
- [30] J. Li, G. Chen, Y. Zhu, Z. Liang, A. Pei, C.-L. Wu, H. Wang, H. R. Lee, K. Liu, S. Chu, Y. Cui, *Nat. Catal.* **2018**, 1, 592.
- [31] R. Shi, J. Guo, X. Zhang, G. I. Waterhouse, Z. Han, Y. Zhao, L. Shang, C. Zhou, L. Jiang, T. Zhang, *Nat. Commun.* **2020**, 11, 3028.
- [32] J. R. Lakowicz, *Principles of Fluorescence Spectroscopy*, 2nd ed., Springer, New York, NY **1999**.
- [33] D. Magde, G. E. Rojas, P. G. Seybold, *Photochem. Photobiol.* **1999**, 70, 737.
- [34] K. Okabe, N. Inada, C. Gota, Y. Harada, T. Funatsu, S. Uchiyama, *Nat. Commun.* **2012**, 3, 705.
- [35] D. McLaughlin, M. Bierling, R. Moroni, C. Vogl, G. Schmid, S. Thiele, *Adv. Energy Mater.* **2020**, 10, 2000488.
- [36] A. Bulan, J. Kintrup, N. Schmitz, A. Karpenko, J. Aßmann, *US9714472B2*, **2017**.
- [37] F. Mugele, J. C. Baret, *J. Phys. Condens. Matter* **2005**, 17, 28.
- [38] A. Forner-Cuenca, V. Manzi-Orezzoli, J. Biesdorf, M. E. Kazzi, D. Streich, L. Gubler, T. J. Schmidt, P. Boillat, *J. Electrochem. Soc.* **2016**, 163, F788.
- [39] V. Parry, G. Berthomé, J.-C. Joud, *Appl. Surf. Sci.* **2012**, 258, 5619.
- [40] A. Quinn, R. Sedev, J. Ralston, *J. Phys. Chem. B* **2005**, 109, 6268.
- [41] F. Bienen, M. C. Paulisch, T. Mager, J. Osiewacz, M. Nazari, M. Osenberg, B. Ellendorff, T. Turek, U. Nieken, I. Manke, K. A. Friedrich, *Electrochem. Sci. Adv.* **2022**, e2100158, <https://doi.org/10.1002/elsa.202100158>.
- [42] D. Bohra, J. H. Chaudhry, T. Burdyny, E. A. Pidko, W. A. Smith, *ChemRxiv* **2020**, 1, <https://doi.org/10.26434/chemrxiv.13073348.v1>.
- [43] N. Gupta, M. Gattrell, B. MacDougall, *J. Appl. Electrochem.* **2006**, 36, 161.